geosciences

MDPI

Article

Strength Equivalence of Two Stiffness Calibrations in Particle Flow Code: An Insight from Micro-Cracking Evolution

Jiao Ye, Fujie Dai and Peng Tang *

Jiangxi Provincial Key Laboratory of Low-Carbon Processing and Utilization of Strategic Metal Mineral Resources, School of Mining Engineering, Jiangxi University of Science and Technology, Ganzhou 341000, China; 9120212038@jxust.edu.cn (J.Y.); 1120220343@mail.jxust.edu.cn (F.D.)

* Correspondence: peng.tang@jxust.edu.cn; Tel.: +86-180-8108-6533

Abstract

Geohazards in rock mass are essentially results of fracturing evolution. Regarding deeper exploration, to better contribute to evaluating and predicting instability, Particle Flow Code (PFC) has gained increasing popularity because of its logical resemblance in simulating rock composition and cracking processes. However, micro-parameter calibrations in PFC mainly focus on both the peak strength and macroscopic cracks in many previous, as well as current, studies, resulting in the existence of two widely used yet distinct strategies in stiffness calibration. The first is to ensure the consistency of the elastic modulus, and the second is to ensure the deformation consistency at peak-stress states. Do these two stiffness calibrations have a strength equivalence? To explore it, several rock mechanical tests—with and without confining pressures and a pre-existing flaw—were numerically conducted using PFC for two materials produced by these two distinct stiffness-calibration strategies. The results demonstrate that the two stiffness calibrations can yield equivalent strength parameters, including tensile strength, cohesion, and internal friction angle. This strength equivalence could be attributed to the evolutionary process of micro-crack initiation, accumulation, nucleation, and global failure (coalescence). Fracture mechanics analysis demonstrates that crack initiation is independent of the elastic modulus and marginally influenced by Poisson's ratio, leading to a negligible impact of stiffness-calibration distinction on crack-initiation stress. Subsequent micro-crack accumulation follows a nearly identical non-linear increasing trend, with a high consistency of spatial distributions in stress concentration, displacement gradient, and strain localization. As a result, the near-identical structural logic in micro-crack nucleation results in failure-pattern consensus and governs the macro-scale strength equivalence of these two distinct stiffness-calibration strategies. These findings could help us to better comprehend those previous, as well as current, research results based on the two stiffness-calibration strategies.

Keywords: PFC simulation; stiffness calibration distinction; strength equivalence; evolutionary mechanism

Check for updates

Academic Editors: Wei Shen, Jian Guo, Qiang Li and Zhitian Qiao

Received: 21 June 2026
Revised: 24 July 2026
Accepted: 30 July 2026
Published: 1 August 2026

Copyright: © 2026 by the authors. Licensee MDPI, Basel, Switzerland. This article is an open access article distributed under the terms and conditions of the Creative Commons Attribution (CC BY) license.

1. Introduction

Geohazards presenting as rock mass instabilities in slopes [1,2] and tunnels [3] are essentially results of rock fracturing evolution. Once the capability of resisting failures, i.e., strength, is reached by applied stress, sudden brittle failure will occur along with a through-going macro-fracture surface [4], which may cut through a rock bridge between pre-existing non-persistent fractures [5]. Thus, investigating the internal processes of rock

fracture development, including initiation, propagation, nucleation, and coalescence [6,7], is of importance for understanding instability mechanisms and developing prediction models. But they are challenging to reveal only by the combination of field investigations and laboratory experiments, especially at the micro-cracking scale. In contrast, numerical simulation methods, including finite element methods (FEMs) [8,9], the discrete element methods (DEMs) [10,11], and coupled methods (FDEMs) [12,13], have gradually become a key supplement. Among these methods, bonded particle models (BPMs) have become increasingly popular because of advantages in simulating fracture networks [14], dealing with crack growth [15,16], and exploring various influencing factors [17,18].

PFC is one of the BPMs, the bonded particles of which logically resemble mineral grains that are cemented in rock. It bridges the gap between laboratory results and further exploration [19,20]. But directly determining micro-properties at the mineral scale is not sufficiently feasible in the laboratory. Therefore, micro-parameters are often determined by calibration based on the trial-and-error method. The standard recommended by Potyondy and Cundall [21] is to mimic the macro-scale mechanical behaviors observed in a laboratory [16,22]. The stress–strain curve of a rock specimen is a focus during micro-parameter calibration [23] since it can directly indicate the features in stiffness and strength (i.e., capabilities of resisting deformation and failure in rock). In a stress–strain curve, despite stiffness change produced by crack-closure behaviors being able to be reproduced in PFC, profiting from recent advances [24], there mainly exist two widely used yet distinct strategies for stiffness calibration in various studies. The first strategy is to ensure the consistency of the elastic modulus, as presented in the works of [25–30], and others. The second strategy is to ensure the deformation consistency at peak-stress states, as presented in the works of [18,31–34] and others. Do these two stiffness calibration strategies result in equivalent strength performance, and what causes this result?

In order to answer these questions, this paper employed PFC to perform common mechanical tests for the two widely used yet distinct stiffness-calibration materials. Direct tension tests and triaxial compression tests were conducted to compare tension and shear strength parameters. Further evolution mechanism exploration was performed by analyzing the cracking progression in samples with a pre-existing notch. The results demonstrate that the simulated rock strength responses exhibit equivalence across two calibration strategies, which stems from the negligible effect of stiffness calibration distinction on micro-crack initiation, accumulation, stress concentration, strain topology, and failure patterns.

2. Materials Produced by Two Stiffness Calibration Strategies

To ensure the validity of numerically simulating rock in this study, sandstone [35] was selected as the reference to establish simulation materials. The uniaxial compressive strength σ_c is 117.6 MPa, and its stress–strain curve is shown in Figure 1a as a bold, black solid line. An approximate concave arc is readily seen during the crack-closure stage, which is the first non-linear section occurring prior to point A_0 in Figure 1a. This phenomenon is mainly produced by stiffness changes with the closure of pre-existing micro-cracks and is currently able to be accurately simulated in PFC [24]. A notable linear section between points A_0 and B_0 in Figure 1a makes it easy to identify as the elastic deformation stage. Stable and unstable crack growths [36] constitute the second non-linear section in the pre-peak curve between points B_0 and C_0 in Figure 1a. Global failure eventually occurs after the peak stress. It is these two non-linear sections that result in the existence of two calibration strategies.

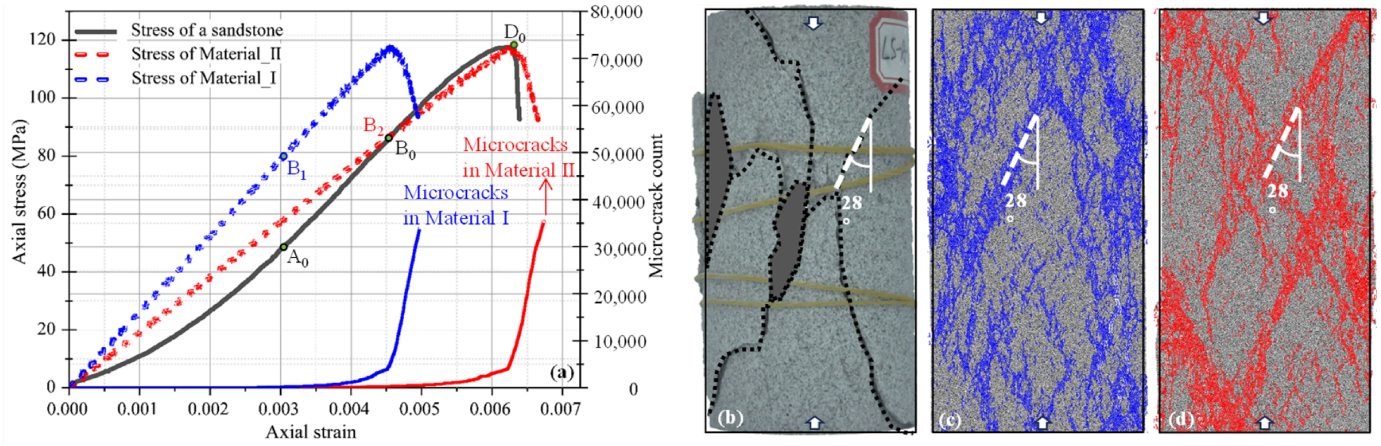


Figure 1. Calibration based on uniaxial compression results: (**a**) Curves of stress, strain, and micro-crack count; (**b**) ultimate failure of sandstone tested by [35]; (**c**) ultimate failure of Material I with blue micro-cracks; (**d**) ultimate failure of Material II with red micro-cracks.

2.1. Micro-Parameter Calibration

Due to the rigidity of particles [37], contact models in PFC are crucial to simulate rock mechanical behaviors [38], which have evolved from the widely used parallel-bonded model (PBM) to the flat-joint model (FJM) [21,39]. The reason lies in three intrinsic deficiencies of PBM [40]: (1) a higher ratio of tensile to compressive strength, (2) a lower friction angle, and (3) a lower Hoek–Brown constant m_i. Consequently, FJM was selected in this research. More details about FJM can be found in [37] and later versions. During micro-parameter calibration process, materials are treated as homogeneous, and deformation occurs only at contacts. Four walls confine the specimen during generation. The side walls are removed for loading, and the top and bottom walls then move toward each other at ± 0.1 m/s. A random seed of 10,001 and a normal damping ratio of 0.5 are employed for particle generation. The damping coefficient is 0.7 during generation and 0.1 during loading. Bonds are activated when the particle gap falls below 0.5×10^{-4} m. To determine the target micro-parameters, the trial-and-error method [21] was carried out. For both the stress–strain curve feature and macro failure, by matching the simulated responses with the experimental results of the sandstone, micro-parameters of Materials I and II in this research were obtained and are shown in Table 1.

Table 1. Micro-parameters of Materials I and II in PFC.

Parameter	Value	Parameter	Value
Type of particle	Disk	Linear contact modulus (GPa)	(19.8) 14.4
Density (kg/m^3)	2650	Flat joint contact modulus (GPa)	(19.8) 14.4
Minimum radius (mm)	0.1	Linear contact stiffness ratio	1
Size ratio	2.5	Flat joint contact stiffness ratio	1
Porosity ratio	0.1	Flat joint contact tensile strength (MPa)	18.9
Damping coefficient	0.1	Flat joint contact cohesion (MPa)	(56.91) 56.94
Friction coefficient	0.577	Flat joint contact friction angle (°)	(10.64) 10.8

Footnote: Values for Materials I and II are in and out parentheses, otherwise they are not different.

2.2. Uniaxial Compression Behaviors

In terms of the axial stress–strain curve of the tested sandstone, the end of the elastic deformation stage was the onset of stable crack growth stage, marked by a clear shift from linearity to non-linearity (Figure 1a). For the axial stress–strain curve of Materials I and II, the onsets of stable crack growth were identified by the generation of the first

micro-crack in Figure 1a, corresponding to crack-initiation stress [41]. Although the peak-strength consistency has been manually controlled by micro-parameter calibration, there is still a difference for crack-initiation stresses, i.e., the onsets of stable crack growth. The crack-initiation stress of Material II is nearly consistent with that of the laboratory-tested sandstone (please see Points B_2 and B_0 in Figure 1a), yet crack-initiation stress and strain in Material I are both significantly lower than those of the laboratory-tested sandstone (please see Points B_1 and B_0 in Figure 1a), demonstrating that Material II may be more appropriate to simulate crack initiation than Material I. According to the slope of the pre-peak curves, the deformation moduli presented in Figure 1 are 25.9 GPa and 18.9 GPa for Materials I and II, respectively; the corresponding Poisson's ratios are 0.09 and 0.05. In terms of the micro-cracks, Materials I and II yield similar results (Figure 1c,d). The macro-fractures resulting from micro-crack coalescence exhibit a nearly X-shaped pattern with a dip angle of approximately 28°, which are consistent with those of the prototype sandstone tested by [35], as shown in Figure 1b. According to the Riedel shear model [42–44], the approximate dip angle of 28° equals the value of 45–$\varphi/2$, implying $\varphi = 34°$ for PFC Materials I and II and the prototype sandstone.

3. Tension and Shear Strength Responses

In terms of rock, fundamental fracture modes are either tensile or shear. Therefore, for the two stiffness-calibration materials, this section will explore their capabilities of resisting tensile and shear failures, i.e., tension and shear strength responses.

3.1. Tensile Strength

The direct tension tests of Materials I and II were numerically performed. The results show that Materials I and II have the same tensile strength (σ_t) of 10.8 MPa while using the random number seed of 10,001. Furthermore, tension tests were repeated separately with 14 random number seeds from 10,002 to 10,015. Results separate from their total of 15 sets of data present the same means of 12.0 MPa and the same standard deviations of 0.6 MPa, indicating that the two different stiffness calibration strategies can yield a consistent capability to resist tension failure.

3.2. Shear Strength

Cohesion (c) and internal friction angle (φ) are the two parameters that depict shear strength. To investigate the shear strength under various specified confining pressures σ_3 = 0.5, 1, 1.5, 2, 2.5, 3, 3.5, 4, 4.5, and 5 MPa, triaxial compression tests were numerically performed by employing 15 different random number seeds from 10,001 to 10,015 in generating particles of sample. Materials I and II exhibit nearly equal peak axial stresses (σ_{1p}) for each random number seed with each specified σ_3. The c and φ are derived by fitting the linear Mohr–Coulomb criterion, which is $\sigma_{1p} = [(1 + sin\varphi)/(1 - sin\varphi)]\sigma_3 + 2ccos\varphi/(1 - sin\varphi)$, based on the peak axial stresses σ_{1p} under different confining pressures σ_3. A total of 15 sets of shear strength parameters were obtained as shown in Figure 2a. Considering the clear negative correlation between cohesion and friction angle, the multivariate analysis of variance (MANOVA) was employed to conduct joint statistical comparison of cohesion and friction angle. The homogeneity assumptions were verified by Box's M test (M = 0.132, p = 0.989) and Levene's test. The results (Wilks'λ = 0.916, p = 0.308 > 0.05) indicate no statistically significant overall difference in strength parameters between Material I (c = 32.39 ± 1.22 MPa, φ = 33.73 ± 1.46°) and Material II (c = 32.14 ± 1.25 MPa, φ = 33.85 ± 1.51°). Furthermore, the corresponding univariate tests verify that, between Materials I and II, no obvious difference existed in individual cohesion (p = 0.579 > 0.05) and friction angle (p = 0.826 > 0.05). These results indicate that the

two different stiffness calibration strategies can yield a consistent capability to resist shear failure.

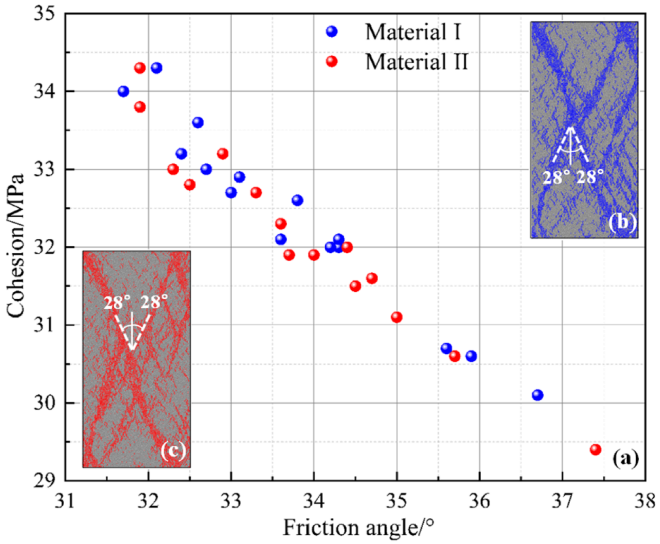


Figure 2. Triaxial compression test results: (**a**) Shear strength parameters of 15 stochastic sample sets; (**b**) typical global failure of Material I (blue micro-cracks); (**c**) typical global failure of Material II (red micro-cracks).

Figure 2b,c presents the macro-crack traces that ultimately lead to global failures. For varying confining pressures, macro-crack traces have a strong similarity between Materials I and II. Confining pressures cause Riedel shears [42–44] to be more sufficiently developed to form more pronounced X-shaped shear fractures in triaxial compression compared to the aforementioned uniaxial compression. Nevertheless, macro-crack dip angles are consistent in uniaxial and triaxial compression, approximating 28° (Figures 1c,d and 2b,c). Therefore, the internal friction angle implied by macro-crack traces is 34°, which is compatible with the mean internal friction angles of 33.7° and 33.9° for Materials I and II, respectively. In summary, two different stiffness calibration strategies can yield a consistent capability to resist shear failure.

4. Mechanism Exploration in Pre-Cracked Samples

Strength responses in rocks are mechanistically related to the evolution of micro-cracks. In this context, rock failure is a progressive process involving the initiation, accumulation, nucleation, propagation, and coalescence of many micro-cracks [45,46]. Micro-cracks act as a source for forming macro-cracks [47] and determining strength feature parameters. Therefore, this section aims at exploring strength response mechanisms by dissecting micro-cracking evolution.

In practical rock engineering, the rock mass consists of both rock and pre-existing cracks. Griffith's theory [48] states that cracking begins at the exact locations of pre-existing cracks, even in rocks that appear to be intact [49]. Thus, a sample with a pre-existing crack is generally selected. For Materials I and II, rock samples including a pre-existing 2a-length crack (Figure 3) were designed to explore the strength response mechanism. According to fracture mechanics [50], tangential stress acting on a pre-existing crack overcomes the pre-crack frictional resistance to produce frictional slip, resulting in tensile stress concentration at the tips of the pre-existing crack, which further induces crack initiation.

The stress intensity factor K_{II} at the pre-existing crack tip can be expressed [51,52] as

$$K_{II} = (\tau_\beta - f\sigma_\beta)\sqrt{\pi a} \quad (1)$$

where a and f are the half-length and friction coefficient of the pre-existing crack, respectively; σ_β and τ_β are the normal and tangential stresses of the pre-existing crack, which are shown in Figure 3.

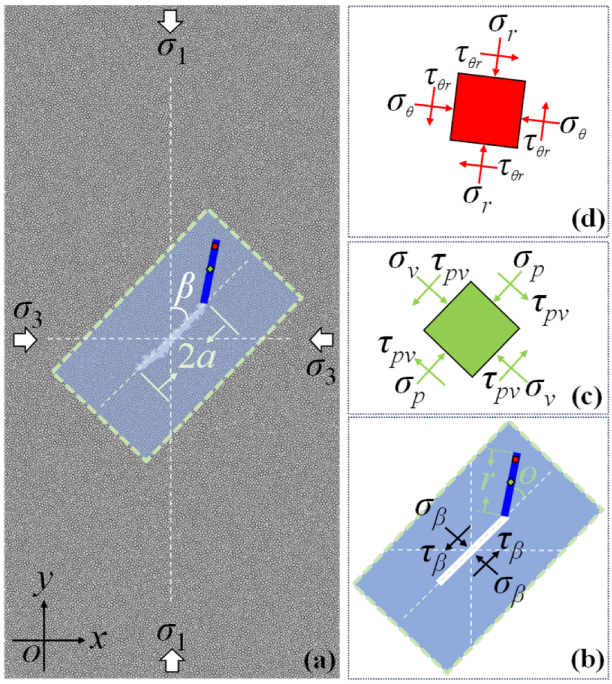


Figure 3. Rock sample containing a pre-existing crack of length 2a, in which the blue line represents cracking initiation. (**a**) general view; (**b**), (**c**), and (**d**) respectively are the local enlargements including mechanical symbols.

The crack initiation criterion at a pre-crack tip can be expressed [52,53] by

$$K_{II} \geq kK_{IC} \tag{2}$$

where kK_{IC} is a critical value for determining crack initiation. It can be regarded as a constant about respective materials.

For the pre-cracked sample under the actions of axial stresses σ_1 and confining stresses σ_3, the corresponding stresses in a pre-existing crack are

$$\sigma_\beta = \sigma_1 \sin^2 \beta + \sigma_3 \cos^2 \beta \tag{3}$$

$$\tau_\beta = (\sigma_1 - \sigma_3) \cos \beta \sin \beta \tag{4}$$

where β is determined by the pre-crack dip angle as shown in Figure 3.

The critical orientation angle β_0 can be obtained by mathematical logic in Equation (5) to form an expression as Equation (6).

$$\begin{cases} \dfrac{\partial K_{II}}{\partial \beta} = 0 \\ \dfrac{\partial^2 K_{II}}{\partial \beta^2} < 0 \end{cases} \tag{5}$$

$$\beta_0 = \frac{1}{2} \arctan(1/f) \tag{6}$$

Equation (6) states that $\beta_0 = 45°$ while $f = 0$. Therefore, if the pre-existing crack does not close during loading, the β of 45° will result in an optimal K_{II}; hence, β was designed

as 45° in this research. Additionally, the pre-crack length and width are ~14 mm and ~1 mm, respectively, in a 100 mm height and 50 mm width sample.

Applying a confining pressure σ_3 of 5 MPa and a gradually increasing axial stress results in a triaxial compression test depicted by a curve as shown in Figure 4. Materials I and II show a nearly consistent peak axial stress of 114.5 MPa.

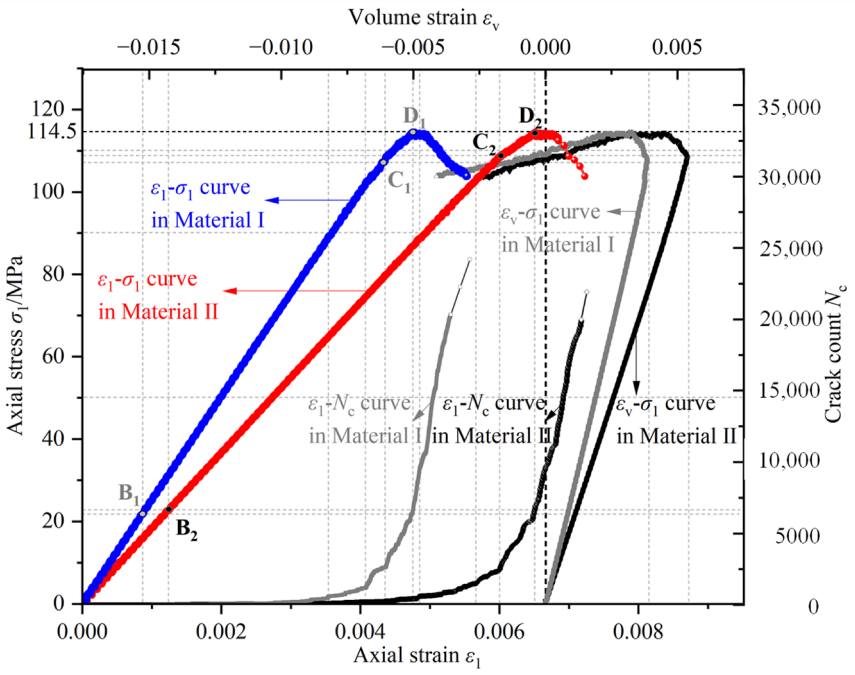


Figure 4. Triaxial compression test results for samples with a pre-existing crack.

Mechanical properties are directly impacted by cracking behaviors [54,55]. To gain a deeper insight into the evolutionary process, the following in-depth analysis of crack initiation, accumulation, and penetration (global failure) was carried out. The onset of the stable crack growth stage was determined by monitoring the cumulative micro-crack count to obtain the crack-initiation stresses of 21.7 MPa and 22.6 MPa, respectively, for Materials I and II (Figure 4). The onset of the unstable crack growth stage was determined by the total volumetric strain reversal [41,56] to obtain the crack-damage stresses of 107.9 MPa and 108.3 MPa, respectively, for Materials I and II (Figure 4).

4.1. Crack Initiation

In the classic fracture mechanics, cracking is categorized into three fundamental types: Type I for an opening mode, Type II for a shearing mode, and Type III for a tearing mode [57]. In the context of plane stress problems, cracking typically occurs under the combination of tensile and shear stresses to form a combination of Type I and II cracks. For the potential new crack near the pre-cracked tip, as shown in Figure 3c, the normal stress components σ_p and σ_v are parallel and perpendicular to the pre-existing crack, respectively. The corresponding shear stress is τ_{pv}. The stress components under the pre-crack influence can be expressed by stress intensity factors as follows:

$$\sigma_p = \frac{K_I}{\sqrt{2\pi r}} \cos\frac{\theta}{2}\left(1 - \sin\frac{\theta}{2}\sin\frac{3\theta}{2}\right) + \frac{K_{II}}{\sqrt{2\pi r}} \sin\frac{\theta}{2}\left(2 + \cos\frac{\theta}{2}\cos\frac{3\theta}{2}\right) \quad (7)$$

$$\sigma_v = \frac{K_I}{\sqrt{2\pi r}} \cos\frac{\theta}{2}\left(1 + \sin\frac{\theta}{2}\sin\frac{3\theta}{2}\right) - \frac{K_{II}}{\sqrt{2\pi r}} \sin\frac{\theta}{2}\cos\frac{\theta}{2}\cos\frac{3\theta}{2} \quad (8)$$

$$\tau_{pv} = \frac{K_I}{\sqrt{2\pi r}} \cos\frac{\theta}{2} \sin\frac{\theta}{2} \cos\frac{3\theta}{2} + \frac{K_{II}}{\sqrt{2\pi r}} \cos\frac{\theta}{2}\left(1 - \sin\frac{\theta}{2} \cos\frac{3\theta}{2}\right) \tag{9}$$

where K_I and K_{II} are respectively type I and II stress intensity factors, which can be expressed as Equations (10) and (1); r and θ are respectively the polar radius and angle, as shown in Figure 3b.

$$K_I = \sigma_\beta \sqrt{\pi a} \tag{10}$$

In the polar coordinate system, the stress components near the pre-crack tip can be expressed by stress intensity factors as follows:

$$\sigma_r = \frac{1}{2\sqrt{2\pi r}}\left[K_I(3 - \cos\theta) \cdot \cos\frac{\theta}{2} + K_{II}(3\cos\theta - 1)\sin\frac{\theta}{2}\right] \tag{11}$$

$$\sigma_\theta = \frac{1}{2\sqrt{2\pi r}} \cos\frac{\theta}{2}[K_I(1 + \cos\theta) - 3K_{II}\sin\theta] \tag{12}$$

$$\tau_{\theta r} = \frac{1}{2\sqrt{2\pi r}} \cos\frac{\theta}{2}[K_I \sin\theta + K_{II}(2 - 3\cos\theta)] \tag{13}$$

where σ_θ, σ_r, and $\tau_{\theta r}$ are respectively the stress components near the pre-crack tip under the polar coordinate system, as shown in Figure 3d.

Considering the fact that initial cracks are predominately tensile fractures, the maximum circumferential tensile stress theory was selected as a fracture criterion. Therefore, the optimal crack-initiation angle θ_i can be determined by the mathematical logic in Equation (14).

$$\begin{cases} \dfrac{\partial \sigma_\theta}{\partial \theta} = 0 \\ \dfrac{\partial^2 \sigma_\theta}{\partial \theta^2} < 0 \end{cases} \tag{14}$$

Combining Equations (12) and (14) obtains Equation (15).

$$K_I \sin\theta_i + K_{II}(3\cos\theta_i - 1) = 0 \tag{15}$$

During the numerical triaxial compression tests for Materials I and II, the pre-crack faces were observed to not close. Therefore, the friction coefficient f equals 0. Due to $\beta = 45°$, integrating Equations (1), (3), (4), (10) and (15) yields

$$\frac{\sigma_1 + \sigma_3}{\sigma_1 - \sigma_3} = \frac{3\cos\theta_i - 1}{\sin\theta_i} \tag{16}$$

Stable crack growth stage onset is the end of the elastic deformation stage. For the elements near the pre-crack tip under elastic conditions, the strain energy density w, i.e., the strain energy per unit area, can be expressed as Equation (17) according to [58].

$$w = \frac{\left(\sigma_p^2 + \sigma_v^2 + 2\tau_{pv}^2\right)}{2E} + \frac{(\tau_{pv}^2 - \sigma_p\sigma_v)\nu}{E} \tag{17}$$

where E is elastic modulus and ν is Poisson's ratio.

The critical stress intensity factor K_{IC} can be expressed as Equation (18) to take into account the mixed fracture behaviors of Type I and II cracks [34].

$$K_{IC} = \frac{1}{2}[K_I(1 + \cos\theta_i) - 3K_{II}\sin\theta_i] \cos\frac{\theta_i}{2} \tag{18}$$

Hence, a critical energy density w_{IC}, quantified by the literature of [58] in Equation (19), can be used to characterize the resistance of crack initiation in a plane stress problem.

$$w_{IC} = \frac{K_{IC}^2}{E} \tag{19}$$

At the pre-crack tip, the crack initiation condition is that the strain energy density w exceeds the critical value w_{IC}. Therefore, integrating Equations (17) and (19) provides a crack initiation criterion such as Equation (20).

$$(\tau_{pv}^2 - \sigma_p\sigma_v)\nu + \frac{\left(\sigma_p^2 + \sigma_v^2 + 2\tau_{pv}^2\right)}{2} \geq K_{IC}^2 \tag{20}$$

Equation (20) indicates that crack initiation does not directly depend on elastic modulus. Fracture toughness K_{IC} can be regarded as a material-feature parameter without difference in Materials I and II. Crack initiation data shown in Figure 4, combined with Equations (1), (3), (4) and (7)–(10), show a definite relation as Equation (21).

$$\tau_{pv}^2 - \sigma_p\sigma_v > 0 \tag{21}$$

In terms of rock, Poisson's ratio, usually within the range of 0.2–0.3, is significantly less than 1. Therefore, crack initiation is more affected by $({\sigma_x}^2 + {\sigma_y}^2 + 2{\tau_{xy}}^2)/2$ than by $({\tau_{xy}}^2 - \sigma_x\sigma_y)\nu$, as shown in the mathematical equation structure of Equation (20), leading to the fact that the stiffness calibration distinction only has a slight impact on crack initiation. Thus, according to the micro-crack monitoring results (Figure 4), the stresses corresponding to crack initiation for the pre-cracked samples of Materials I and II are 21.7 MPa and 22.6 MPa, respectively.

4.2. Crack Development

The development of normalized micro-crack density, defined as the ratio of generated micro-cracks (N_c) to the total potential micro-crack count (N = 43,952, determined by initial contacts), is plotted against the stress ratio (σ_3/σ_1) in Figure 5. Under a constant confining pressure σ_3 = 5 MPa, both Materials I and II exhibit a pronounced non-linear, negative correlation between σ_3/σ_1 and N_c/N. Based on the crack-initiation and crack-damage stresses, the stable crack growth stage is characterized by σ_3/σ_1 ranges of 0.23–0.46 and 0.22–0.46 for Materials I and II, respectively. While the stress ratio σ_3/σ_1 is no less than 0.10, the rate of micro-crack generation stabilizes and approaches an asymptote near zero, indicating a very low rate of micro-crack initiation for both Materials I and II. As the stress ratio σ_3/σ_1 decreases from 0.10, the rate of generating micro-cracks increases significantly. Specifically, both Material I and Material II exhibit a rapid, exponential increase in N_c/N as the stress ratio decreases below a critical threshold of 0.46, indicating an accelerated accumulation of micro-cracks in the unstable crack growth stage. The σ_3/σ_1 of 0.46 corresponding to crack-damage stress could be regarded as a distinct transition point or critical threshold. Once the stress ratio drops below this threshold, the respective materials undergo rapid damage, with N_c/N surging beyond 0.16 to reach peak stresses, indicating that high axial loads drive significant micro-fracturing. The curves for Material I and Material II are virtually coincident in micro-crack accumulation. This remarkable overlap between the data points for Material I (solid blue line in Figure 5) and Material II (dashed red line in Figure 5) suggests that the stiffness calibration diversity does not primarily govern the evolution of micro-crack accumulation.

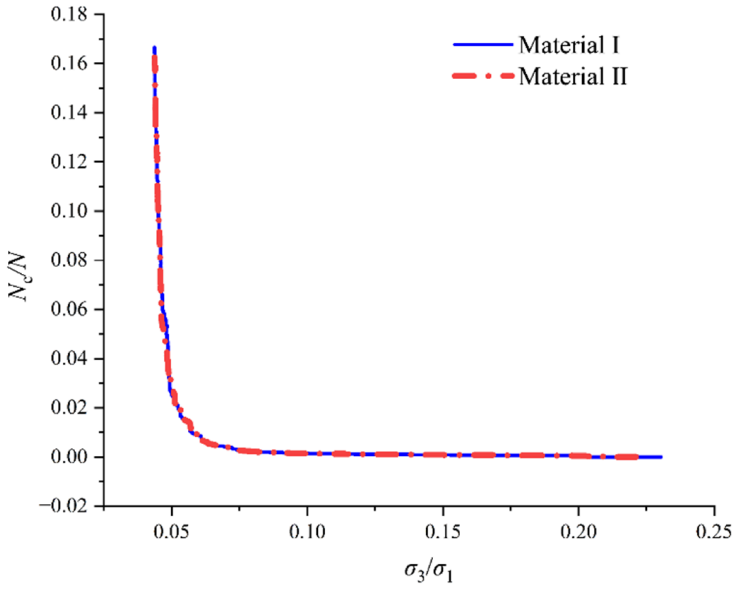


Figure 5. Evolution of N_c/N versus normalized stress σ_3/σ_1. Nc is the generated micro-crack count. N is the total potential micro-crack count (N = 43,952, determined by initial contacts). σ_1 is the applied axial stress and σ_3 is the confining pressure.

To further explore the development of micro-cracks, Figure 6 provides a sequential comparison of Material I (top row) and Material II (bottom row) as they undergo progressive axial loading. Horizontal displacement (δ_x) of each particle, measured in micrometers, is superimposed with the development of micro-cracks (represented by the short black lines) around a pre-existing crack (the central diagonal notch). Color contours represent the magnitude and direction of δ_x, in which positive and negative values indicate rightward and leftward movements, respectively.

During the stage of stable crack growth (e.g., σ_1 = 70 or 105 MPa), both materials exhibit a localized displacement gradient concentrated at the notch tips where micro-cracks initiate. The resulting displacement field displays overall anti-symmetry with respect to the notch. It indicates that the elastic–plastic transition is governed by the nearly identical stress intensity factor geometry, regardless of the specific stiffness of respective materials. During the unstable crack growth stage (i.e., σ_1 = 107.9–114.5 MPa for Material I and 108.3–114.5 MPa for Material II), the materials coalesce into macro-cracks. Those newly formed cracks locally alter the spatial distribution of displacement, which to some extent influences the direction of crack propagation, leading to a difference in crack patterns when σ_1 = 110 MPa. Nevertheless, the global consistency in the process mechanism is maintained between these two materials.

As the smooth color contours break down into fragmented zones, both materials undergo a transition from stochastic micro-cracking to localized micro-cracks. The spatial distribution of micro-cracking follows a near-identical structural logic in both materials. At the peak stress state (σ_1 = 114.5 MPa), although micro-cracks in Material I expand more extensively to present a more noticeable penetration trend than those in Material II, both materials exhibit a relatively clear shear band, where the coalescence of micro-cracks leads to a macroscopic discontinuity in the displacement field, heralding the formation of diagonal shear fractures that eventually bisect the specimen. In addition, macro-crack penetration directions are highly consistent between the two materials.

Despite discrepancies in absolute displacement magnitudes of the particles, Materials I and II exhibit phenomenological consistency in their micro-crack accumulation. In the pre-peak development process, both materials exhibit a highly consistent anti-symmetric distribution of δ_x, which serves as the nucleation site for micro-cracks. Although crack

patterns appear more localized in Material I than in Material II, the transition from localized tip-straining to global shear-banding follows a uniform evolutionary trajectory. These consistencies suggest that the geometric configuration of the internal flaw exerts a far more dominant influence on the failure morphology than the stiffness calibration diversity.

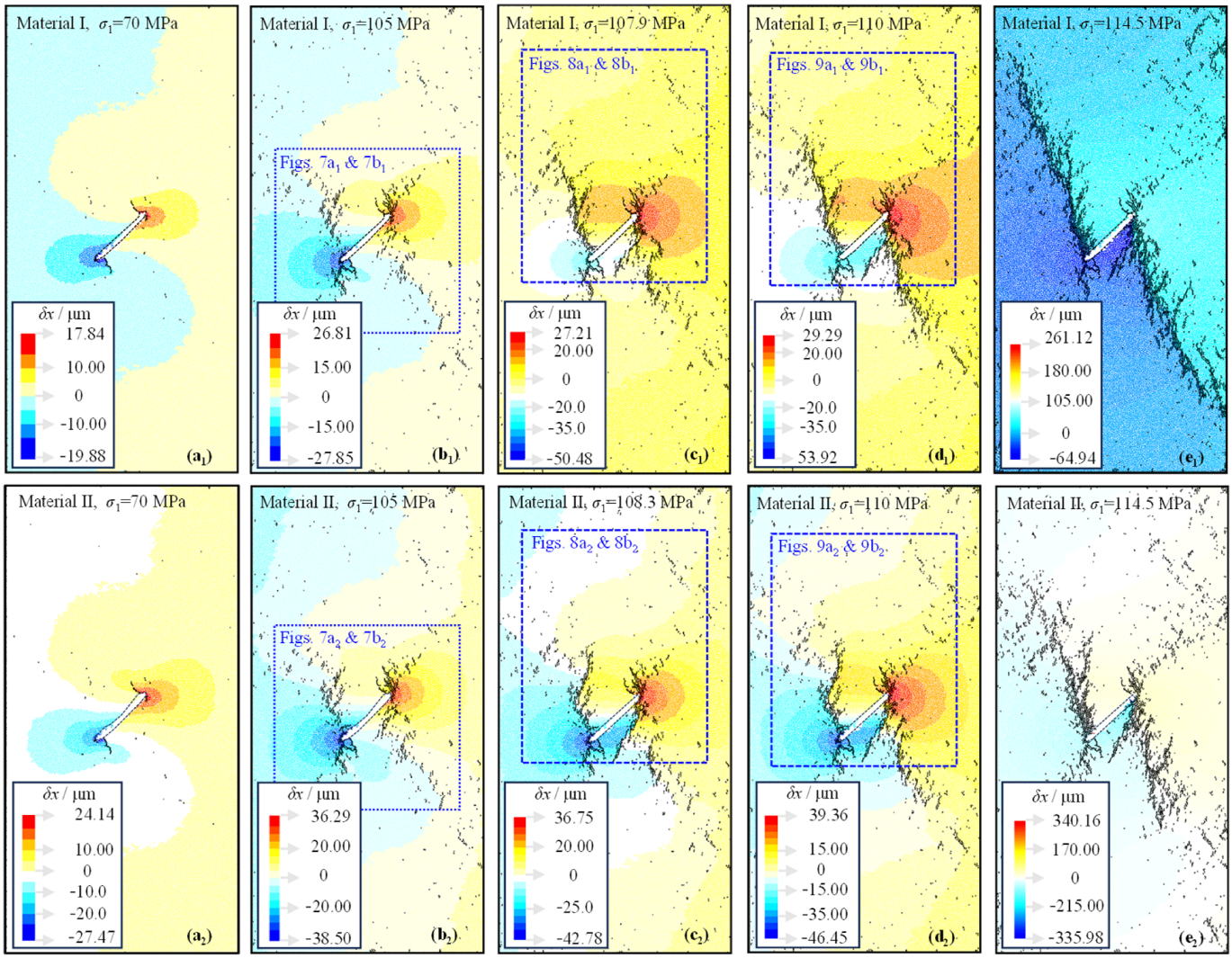


Figure 6. Horizontal displacement fields in Materials I (**a$_1$**–**e$_1$**) and II (**a$_2$**–**e$_2$**). Positive and negative values denote rightward and leftward displacements, respectively. The pre-existing crack is created via particle deletion. Micro-cracks are indicated by short black lines.

Based on elastoplastic theory, both horizontal normal strain ε_h and shear strain γ_{hv} can be directly derived from the horizontal and vertical displacement components (δ_x and δ_y). In this research, the calculated strain fields are presented in Figures 7–10.

In the stage of stable crack growth, wing cracks are the predominant mode of macro-cracks [22,59]. Figure 7 shows the εh and γhv for both materials at σ_1 = 105 MPa. These strain fields correspond to the region surrounding the pre-existing notch, as shown in Figure 6. The ε_h reveals nearly identical stress concentration points at the crack tips, which drive the generation of micro-cracks in both materials. Shear strain contours of both materials exhibit a butterfly-shaped distribution surrounding the pre-existing notch. Although Material II shows a slightly higher peak strain compared to Material I, strain fields across both materials exhibit high consistency in their spatial distributions.

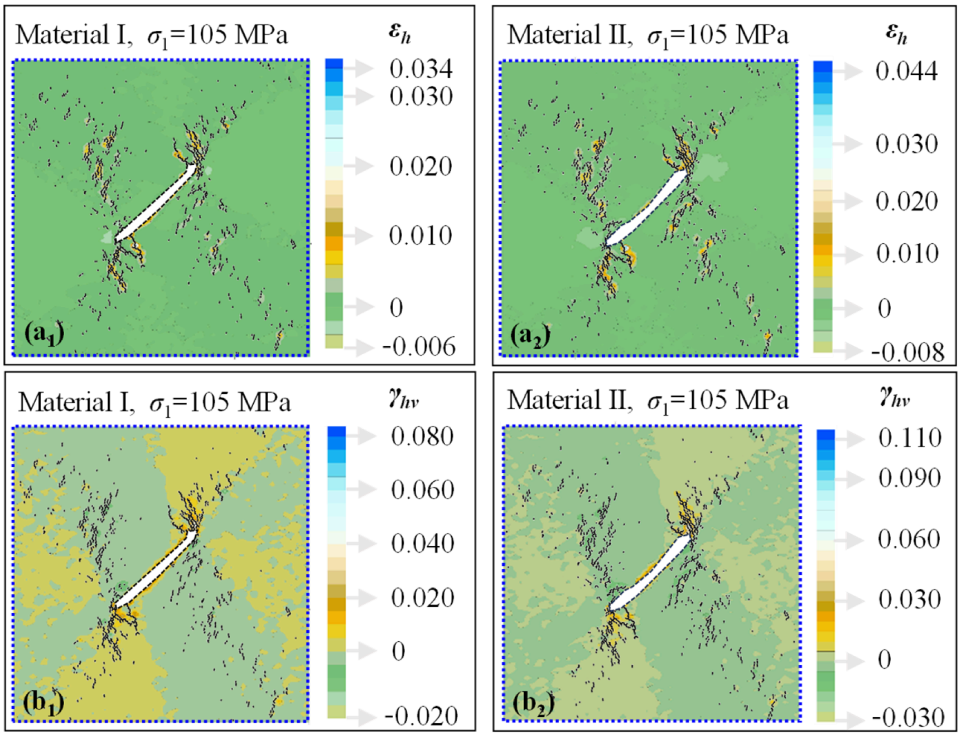


Figure 7. Horizontal normal strain (ε_h) and shear strain (γ_{hv}) for the two materials at σ_1 = 105 MPa. Positive and negative values of εh denote tensile and compressional strains, respectively. These strain fields correspond to the region surrounding the pre-existing notch as shown in Figure 6.

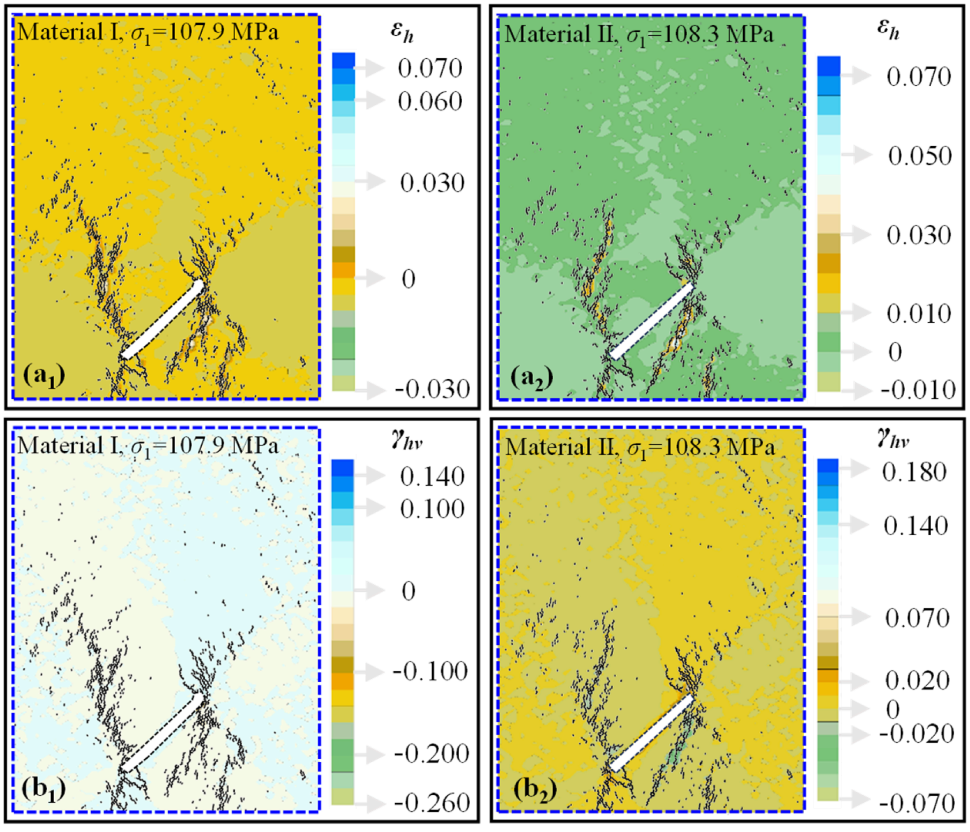


Figure 8. Horizontal normal strain (ε_h) and shear strain (γ_{hv}) for the two materials at the transition stress from stable to unstable crack growth. Positive and negative values of ε_h denote tensile and compressional strains, respectively.

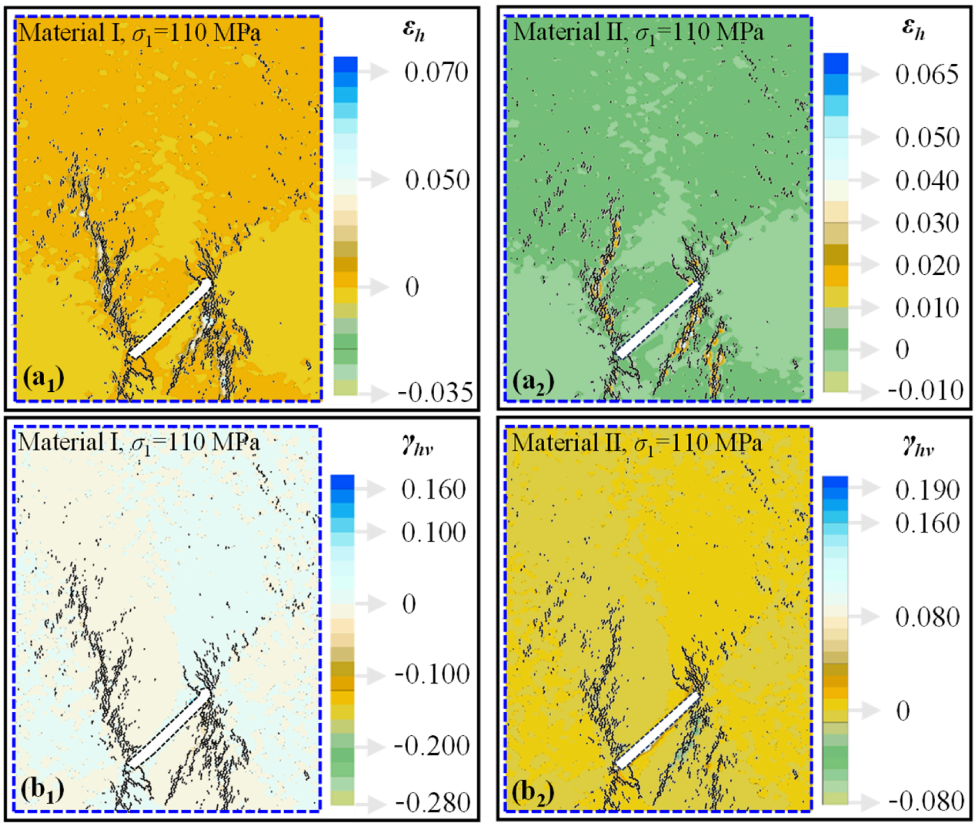


Figure 9. Horizontal normal strain (ε_h) and shear strain (γ_{hv}) for the two materials at σ_1 = 110 MPa.

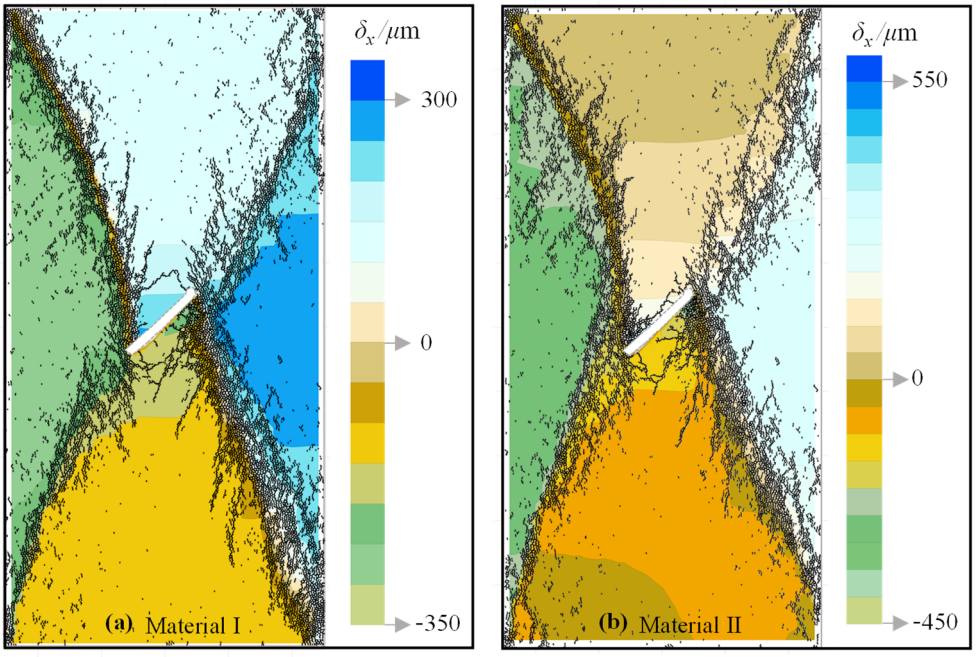


Figure 10. Horizontal displacement (δ_x) at a post-peak σ_1 of 0.7 times peak strength. Positive and negative values denote rightward and leftward displacements, respectively.

At the crack-damage stress state (long-term strength points), micro-cracks begin to coalesce, and the material enters a state of accelerated damage. The propagation of wing cracks tends to cease, whereas oblique secondary cracks are predominant macro-cracks [22,59]. Figure 8 shows the εh and γhv at the stress transition from stable to unstable crack growth. These strain fields correspond to the region surrounding the pre-existing

notch as shown in Figure 6. The εh fields undergo a significant expansion compared to previous stages. Tensile strain concentrations are no longer confined to the notch tips but expand into broader zones. Material I reaches a peak ε_h of 0.07, while Material II reaches a similar peak, indicating a convergence in extensional behavior at the point of progressive failure. Although the magnitude of γ_{hv} in Material II (0.18) is significantly higher than that in Material I (0.14), the γ_{hv} spatial distributions in both materials imply the formation of conjugate shear bands radiating from the notch. The spatial topologies of the strain concentrations remain consistent at the crack-damage stress states.

In the stage of unstable crack growth, Figure 9 shows the εh and γ_{hv} for both materials at σ_1 = 110 MPa. These strain fields correspond to the region surrounding the pre-existing notch as shown in Figure 6. Tensile strain zones in both materials, revealed by ε_h, have more extensive tensile dilations compared to those at the crack-damage stress state. Therefore, zones of high ε_h concentration are found extending from the notch tips to the specimen boundaries, indicating that stress redistribution spreads across wider zones in both materials. The γ_{hv} distributions contribute to the gradual maturation of conjugate shear bands, which serve as the structural framework for macroscopic failure. As micro-cracks develop from localized to specimen-scale phenomena, both materials are in the transition from a continuum to a potentially discontinuous state. The intensification of shear localization in Materials I and II, coupled with the fragmented topology of the strain contours, signifies the imminent completion of global failure.

4.3. Global Failure

Global failure is essentially a transition from macroscopic continuity to discontinuity, which is the result of damage accumulation, stress redistribution, and macroscopic-scale fracture [60]. The contour plots in Figure 10 illustrate the δ_x measured in micrometers at the post-peak stress state of $0.7\sigma_{1p}$. The short black lines superimposed on the displacement fields represent micro-cracks (bond breakages in PFC materials). Both materials exhibit very similar X-shaped fractures. Although Material II exhibits a higher density and wider distribution of micro-cracks compared to Material I, conjugate shear bands in both materials are produced by the coalescence of micro-cracks that intersect at the pre-existing notch. Despite Material II exhibiting a higher absolute displacement magnitude compared to Material I, both δ_x fields in Materials I and II are relatively symmetric, indicating a balanced shear failure. Finally, both materials share a consistent failure pattern characterized by conjugate shear fracturing.

5. Discussion

Considering the fact that micro-crack development, that is, from their start to accumulation [61], is intrinsically linked to both stiffness and strength, it is necessary to take into account the possible influence of stiffness on strength. Cracking mechanisms are closely linked to peak resistances in both shear and tension [55,62]. Our findings support this link and show that the two widely used stiffness calibration strategies in PFC exhibit high consistency in peak resistance and fracture evolutions. To some extent, they may provide evidence that the two stiffness calibration strategies might be able to equivalently investigate rocky slope instability, including slope stability evaluation and potential slip surface prediction.

To verify this point, slope models were constructed as illustrated in Figure 11. The total height of the model slope was established at 450 m, with a vertical distance of 350 m from the landslide shear exit to the slope crest. The potential sliding surface is defined by two pre-existing rupture surfaces, each 120 m in length, connected by an intervening rock bridge with a length of 160 m. When constructing the numerical mod-

els using the microscopic parameters of PFC Materials I and II, particles with radii of 0.9–1.0 m were employed. The safety factor was determined using the gravity increase method, with the formation of a continuous macro-shear surface serving as the failure criterion. Gradually increasing the gravity multiplier until just meeting the failure criterion is the way to get a slope safety factor in this study. For the purpose of bring into correspondence with the two calibrated rock materials, rock mass strength degradation resulting from discontinuities and disturbance in nature is not considered by the Hoek–Brown Failure Criterion [63] in this study. Therefore, slope safety factors are one order of magnitude higher than physically reasonable values for natural slopes. But results show that slope safety factors for Material I (22.54) and Material II (22.46) are nearly identical to one decimal place, indicating that the two stiffness calibration strategies can equivalently evaluate rocky slope stability.

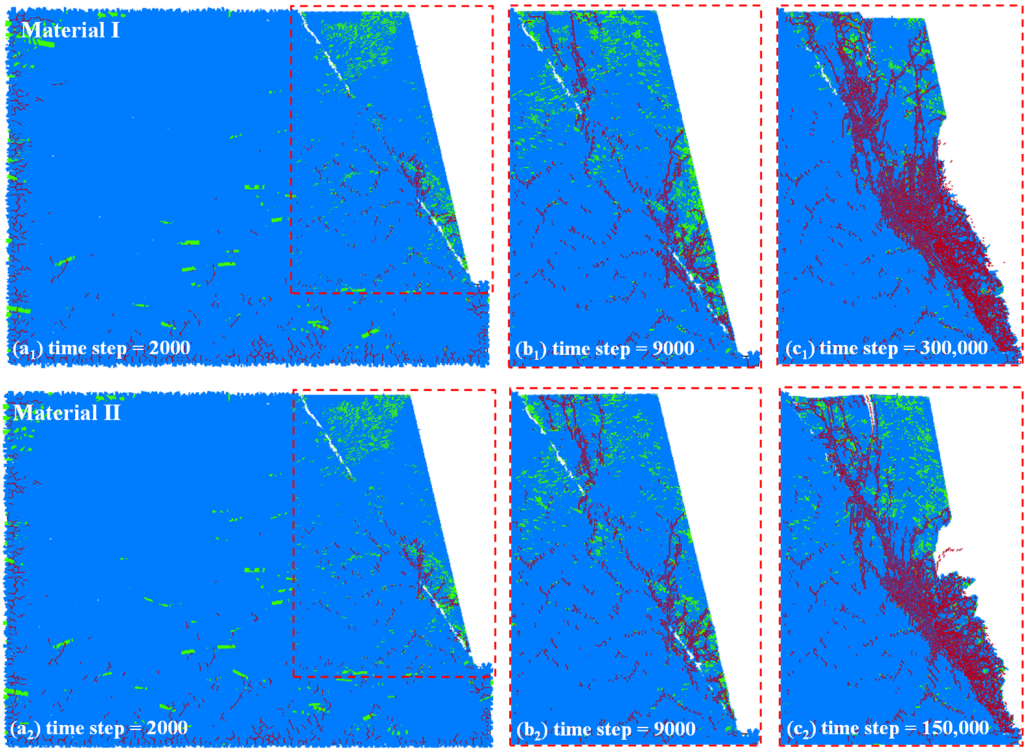


Figure 11. Cracking evolution in slopes of two stiffnesses. Red segments represent micro-cracks, and green segments represent the mesoscopic tensile force chains.

Furthermore, the localized fracture evolution follows a highly synchronized path regardless of the respective materials. The green line segments in Figure 11 represent mesoscopic tensile stress concentrations. In both materials, at a time step of 2000, these concentrations appear primarily along the potential slip path and near the boundaries of the rock bridge. The spatial density and orientation of these tensile stress hotspots are virtually indistinguishable between Figure 11(a_1,a_2), indicating that stress redistribution is governed by the geometric configuration of the rock bridge rather than the material stiffness diversity. The red line segments in Figure 11 represent cracks produced by bond breakages in PFC. As time steps progress from 9000 to the final failure, cracks propagate from the tips of the pre-existing rupture surfaces (Figure 11(b_1,b_2)) toward the center of the rock bridge (Figure 11(c_1,c_2)). Both materials exhibit an en-echelon cracking pattern. However, Materials I and II reach full through-going fracture at time steps of 300,000 and 150,000, respectively. Although PFC time steps do not correspond to physical time, it suggests that the ultimate stability factor and failure geometry are consistent, but the fracture kinetics (rate of crack accumulation) differ. This is only a difference in deformation

as a result of stiffness-calibration distinction, not a contradiction to strength equivalence. The consistency of rock-bridge fracture processes in simulating landslides reinforces the theme of mechanical consistency between Materials I and II, without a significant influence from the two widely used stiffness calibration strategies. It suggests that, in terms of the two stiffness calibrations, strength equivalence lies at both laboratory and field scales. These findings could help us to better comprehend those previous, even current, research results based on the two stiffness calibration strategies.

6. Conclusions

Strength responses produced by two previously widely used yet distinct stiffness-calibration strategies in PFC—namely maintaining the consistency of elastic modulus (Material I) or the deformation consistency at peak-stress states (Material II)—were compared and systematically explored. The following findings were obtained:

(1) The two stiffness-calibration strategies demonstrate strength equivalence in tensile strength, cohesion, and internal friction angle, implying their equivalent capability in resisting tensile and shear failures.

(2) The process mechanism of strength equivalence could be attributed to the failure-pattern consensus governed by the near-identical evolution of micro-cracks. Fracture mechanics analysis demonstrates that crack initiation is independent of the elastic modulus and marginally influenced by Poisson's ratio, resulting in being nearly identical in crack initiation. The subsequent micro-crack accumulation also follows a nearly identical non-linear increasing trend, with a high consistency of spatial distributions in stress concentration, displacement gradient, and strain localization.

Author Contributions: Software, Data Curation, Visualization, Formal Analysis, Investigation, Writing—Original Draft, J.Y.; Investigation, Validation, Formal Analysis, Writing—Review and Editing, F.D.; Conceptualization, Resources, Methodology, Writing—Original Draft, Investigation, Supervision, P.T. All authors have read and agreed to the published version of the manuscript.

Funding: This research was funded by the National Natural Science Foundation of China (Grant No. 42502274), Jiangxi Provincial Natural Science Foundation (Grant No. 20242BAB20150).

Data Availability Statement: The data that support the findings of this study are available from the corresponding author upon reasonable request.

Acknowledgments: We would like to express our sincere gratitude to all students (Shou-Sheng Sheng, Xuan Tian, and Xin Zhou) who have helped us during this study and the writing of this paper. During the preparation of this manuscript, the authors used several AI-assisted tools/services (e.g., DeepSeek, DouBao, Qwen, ERNIE Bot, and so on) to improve content organization, polish language, and strengthen readability. After using these tools/services, all authors reviewed and reedited the content with critical thinking and take full responsibility for the manuscript.

Conflicts of Interest: The authors declare no conflicts of interest. The funders had no role in the design of the study; in the collection, analyses, or interpretation of data; in the writing of the manuscript; or in the decision to publish the results.

References

1. Chen, G.; Sun, X.; Xu, Q.; Zeng, S.; Xing, J.; Feng, X.; Liu, F. Rock-mass heterogeneous rheological properties caused the formation of deep tension fractures. *Geomech. Energy Environ.* **2026**, *38*, 100545. [CrossRef]
2. Qin, C.; Chen, G.; Wang, J.; Zhang, G. Stability analysis of slopes with stepped failure using a vector sum particle flow method. *Bull. Eng. Geol. Environ.* **2024**, *83*, 409. [CrossRef]
3. Liu, H.; Wang, J.; Cheng, P.; Zhu, P.; Liu, Q.; Guo, T.; Pu, C.; Liao, Q.; Zhang, P. Stability analysis and fracture evolution in topographical bias tunnels within layered rock masses: Insights from FDEM simulation. *Comput. Geotech.* **2026**, *197*, 108251. [CrossRef]

4. Tang, P.; Chen, G.; Huang, R.; Zhu, J. Brittle failure of rockslides linked to the rock bridge length effect. *Landslides* **2019**, *17*, 793–803. [CrossRef]
5. Chen, G.; Gu, L.; Xu, Q.; Yang, X.; Zhao, Y. Shear properties of non-persistent coplanar fractured hard rocks under normal stress unloading. *J. Rock Mech. Geotech.* **2025**, *17*, 3593–3608. [CrossRef]
6. Liu, Z.; Ma, C.; Xie, W. Fracture characteristics and mechanism of single fissure sandstone under triaxial extension: Insights from experiments and simulations. *Theor. Appl. Fract. Mec.* **2026**, *146*, 105761. [CrossRef]
7. Liu, Z.; Ma, C.; Wei, X.; Yi, W.; Lei, J. Failure mechanisms of coarse-grained sandstone under pure mode I/II loading: Insights from energy evolution and acoustic emission. *Nondestruct. Test. Eval.* **2025**, *40*, 4415–4435. [CrossRef]
8. Yue, Z.; Chen, S.; Tham, L. Finite element modeling of geomaterials using digital image processing. *Comput. Geotech.* **2003**, *30*, 375–397. [CrossRef]
9. Chen, G.; Zheng, S.; Zhu, J.; Wang, W.; Feng, W. A quantitative display index that considers tensile failure to predict the full sliding surface of a landslide. *Landslides* **2020**, *17*, 471–482. [CrossRef]
10. Wang, P.; Yin, Z.; Hicher, P.; Cui, Y. Micro-mechanical analysis of one-dimensional compression of clay with DEM. *Int. J. Numer. Anal. Met.* **2023**, *47*, 2706–2724. [CrossRef]
11. Zheng, Z.; Li, S.; Zhang, Q.; Tang, H.; Liu, G.; Pei, S.; Lu, G. True triaxial test and DEM simulation of rock mechanical behaviors, meso-cracking mechanism and precursor subject to underground excavation disturbance. *Eng. Geol.* **2024**, *337*, 107567. [CrossRef]
12. Liu, H.; Zhu, P.; Liu, Q.; Jiang, Y.; Shao, Z.; Lin, Q.; Yang, Y. Mesoscopic numerical modeling of Soil-Rock mixtures: Investigation of mechanical behavior and failure mechanisms based on FDEM. *Comput. Geotech.* **2025**, *186*, 107455. [CrossRef]
13. Liu, H.; Zhu, P.; Liu, Q.; Sun, C.; Yang, Y.; He, G.; He, C. Equivalent Nodal Intensity-Based Contact Model for 3D Finite-Discrete Element Method in Rock Fracturing Analysis. *Rock Mech. Rock Eng.* **2025**, *58*, 6059–6086. [CrossRef]
14. Zhou, C.; Rui, Y.; Qiu, J.; Wang, Z.; Zhou, T.; Long, X.; Shan, K. The role of fracture in dynamic tensile responses of fractured rock mass: Insight from a particle-based model. *Int. J. Coal Sci. Technol.* **2025**, *12*, 39. [CrossRef]
15. Chen, G.; Tang, P.; Huang, R.; Wang, D.; Lin, Z.; Huang, D. Critical tension crack depth in rockslides that conform to the three-section mechanism. *Landslides* **2020**, *18*, 79–88. [CrossRef]
16. Cen, D.; Liu, C.; Liu, C.; Huang, D. Crack propagation mechanism of single- and double-flawed rock specimens under tension–shear stress condition. *Arab. J. Geosci.* **2022**, *15*, 10. [CrossRef]
17. Zhou, C.; Qiu, J.; Karakus, M.; Wang, C.; Feng, F.; Wang, F.; Zhou, T. Unraveling rate-strengthening and fracture-weakening effects in fractured rock masses: A hybrid bonded particle model-discrete fracture network and physics-inspired machine learning framework. *J. Rock Mech. Geotech.* **2026**, *18*, 5254–5541. [CrossRef]
18. Wu, L.; Chen, G.; Xing, J.; Lin, Z. Brittle cataclastic process of fault rocks based on a large-displacement direct shear model realized with DEM. *J. Struct. Geol.* **2022**, *161*, 104641. [CrossRef]
19. Gutiérrez-Ch, J.G.; Senent, S.; Zeng, P.; Jimenez, R. DEM simulation of rock creep in tunnels using Rate Process Theory. *Comput. Geotech.* **2022**, *142*, 104559. [CrossRef]
20. Qin, C.; Chen, G.; Zhang, G. Tension-shear extension criteria used in PFC to reveal a brittle failure of rock bridges in rock slopes with stepped joints. *Eng. Fract. Mech.* **2024**, *295*, 109807. [CrossRef]
21. Potyondy, D.; Cundall, P. A bonded-particle model for rock. *Int. J. Rock Mech. Min.* **2004**, *41*, 1329–1364. [CrossRef]
22. Huang, D.; Cen, D.; Ma, G.; Huang, R. Step-path failure of rock slopes with intermittent joints. *Landslides* **2015**, *12*, 911–926. [CrossRef]
23. Yang, S.; Yin, P.; Zhang, Y.; Chen, M.; Zhou, X.; Jing, H.; Zhang, Q. Failure behavior and crack evolution mechanism of a non-persistent jointed rock mass containing a circular hole. *Int. J. Rock Mech. Min.* **2019**, *114*, 101–121. [CrossRef]
24. Peng, S.; Li, X.; Li, C.; Liang, L.; Huang, L. Crack-closure behavior and stress-sensitive wave velocity of hard rock based on flat-joint model in particle-flow-code (PFC) modeling. *Comput. Geotech.* **2024**, *170*, 106320. [CrossRef]
25. Yoon, J. Application of experimental design and optimization to PFC model calibration in uniaxial compression simulation. *Int. J. Rock Mech. Min.* **2007**, *44*, 871–889. [CrossRef]
26. Yang, X.; Kulatilake, P.H.S.W.; Jing, H.; Yang, S. Numerical simulation of a jointed rock block mechanical behavior adjacent to an underground excavation and comparison with physical model test results. *Tunn. Undergr. Space Technol.* **2015**, *50*, 129–142. [CrossRef]
27. Ozturk, H.; Altinpinar, M. The estimation of uniaxial compressive strength conversion factor of trona and interbeds from point load tests and numerical modeling. *J. Afr. Earth Sci.* **2017**, *131*, 71–79. [CrossRef]
28. Yang, X.; Qiao, W. Numerical investigation of the shear behavior of sandstone materials containing discontinuous joints by utilizing the flat-joint model. *Comput. Geotech.* **2018**, *104*, 69–80. [CrossRef]
29. Haeri, H.; Sarfarazi, V.; Marji, M.F. Static and Dynamic Response of Rock Engineering Models. *Iran. J. Sci. Technol.-Trans. Civ. Eng.* **2022**, *46*, 327–341. [CrossRef]

30. Tang, Y.; Lin, H.; Li, S.; Chen, Y.; Ou, K.; Xie, L. Numerical study of rock bridge shape identification and rock bridge damage mechanism. *Comput. Part. Mech.* **2024**, *11*, 2483–2497. [CrossRef]
31. Kulatilake, P.H.S.W.; Malama, B.; Wang, J. Physical and particle flow modeling of jointed rock block behavior under uniaxial loading. *Int. J. Rock Mech. Min.* **2001**, *38*, 641–657. [CrossRef]
32. Bahaaddini, M.; Sheikhpourkhani, A.M.; Mansouri, H. Flat-joint model to reproduce the mechanical behaviour of intact rocks. *Eur. J. Environ. Civ. Eng.* **2019**, *25*, 1427–1448. [CrossRef]
33. Tang, P.; Chen, G.; Huang, R.; Wang, D. Effect of the number of coplanar rock bridges on the shear strength and stability of slopes with the same discontinuity persistence. *Bull. Eng. Geol. Environ.* **2021**, *80*, 3675–3691. [CrossRef]
34. Cao, P.; Zhou, T.; Ju, Y.; Zhu, J. Mixed mode I/II fracture behavior of CSTBD sandstone specimen under different loading angles. *J. Geomech. Geophys. Geo-Energy Geo-Resour.* **2023**, *9*, 54. [CrossRef]
35. Li, H.; Yang, S.; Yang, Z.; Zhou, X.; Tian, W.; Wang, S. Experimental and numerical study on the mechanical behaviors and crack propagation of sandstone containing two parallel fissures. *Theor. Appl. Fract. Mech.* **2023**, *126*, 103965. [CrossRef]
36. Martin, C.D.; Christiansson, R. Estimating the potential for spalling around a deep nuclear waste repository in crystalline rock. *Int. J. Rock Mech. Min.* **2009**, *46*, 219–228. [CrossRef]
37. Itasca Consulting Group Inc. *PFC Particle Flow Code in 2 Dimensions User's Guide*; Itasca: Minneapolis, MN, USA, 2016.
38. Cundall, P.A.; Strack, O.D.L. A discrete numerical model for granular assemblies. *Geotéchnique* **1979**, *29*, 47–65. [CrossRef]
39. Potyondy, D. *PFC Flat-Joint Contact Model*; Itasca Consulting Group Inc.: Minneapolis, MN, USA, 2012.
40. Wu, S.; Xu, X. A Study of Three Intrinsic Problems of the Classic Discrete Element Method Using Flat-Joint Model. *Rock Mech. Rock Eng.* **2016**, *49*, 1813–1830. [CrossRef]
41. Martin, C.D.; Chandler, N. A The progressive fracture of Lac du Bonnet granite. *Int. J. Rock Mech. Min.* **1994**, *31*, 643–659. [CrossRef]
42. Riedel, W. Zur Mechanik geologischer Brucherscheinungen. *Zentralblatt Mineral. Geol. Paläontologie. Abt. B* **1929**, 354–368.
43. Cho, N.; Martin, C.D.; Sego, D.C. Development of a shear zone in brittle rock subjected to direct shear. *Int. J. Rock Mech. Min.* **2008**, *45*, 1335–1346. [CrossRef]
44. Einstein, H. Physical Modelling in Rock Mechanics and Rock Engineering. *Rock Mech. Rock Eng.* **2024**, *57*, 10187–10204. [CrossRef]
45. Lockner, D.A.; Byerlee, J.D.; Kuksenko, V.; Ponomarev, A.; Sidorin, A. Quasi-static fault growth and shear fracture energy in granite. *Nature* **1991**, *350*, 39–42. [CrossRef]
46. Vu, C.C.; Amitrano, D.; Pl'e, O.; Weiss, J. Compressive failure as a critical transition: Experimental evidence and mapping onto the universality class of depinning. *Phys. Rev. Lett.* **2019**, *122*, 015502. [CrossRef] [PubMed]
47. Zhang, J.; Zhou, X. Fracture process zone (FPZ) in quasi-brittle materials: Review and new insights from flawed granite subjected to uniaxial stress. *Eng. Fract. Mech.* **2022**, *274*, 108795. [CrossRef]
48. Griffith, A.A. The phenomena of rupture and flow in solids. *Philos. Trans. R. Soc. Lond. (Ser. A)* **1921**, *221*, 163–198. [CrossRef]
49. Alava, M.J.; Nukala, P.K.V.V.; Zapperi, S. Size effects in statistical fracture. *J. Phys. D Appl. Phys.* **2009**, *42*, 214012. [CrossRef]
50. Anderson, T.L. *Fracture Mechanics: Fundamentals and Applications*; Taylor and Francis: Boca Raton, FL, USA, 2005.
51. Tada, H. *Stress Analysis of Cracks Handbook*; Del Research Corporation: Hellertown, PA, USA, 1973.
52. Zuo, J.; Li, H.; Xie, H.; Ju, Y.; Peng, S. A nonlinear strength criterion for rock-like materials based on fracture mechanics. *Int. J. Rock Mech. Min.* **2008**, *45*, 594–599. [CrossRef]
53. Cotterell, B.; Rice, J.R. Slightly curved or kinked cracks. *Int. J. Fract.* **1980**, *16*, 155–169. [CrossRef]
54. Haeri, H.; Sarfarazi, V.; Zhu, Z. Effect of normal load on the crack propagation from pre-existing joints using Particle Flow Code (PFC). *Comput. Concr.* **2017**, *19*, 99–110. [CrossRef]
55. Asadizadeh, M.; Moosavi, M.; Hossaini, M.F.; Masoumi, H. Shear strength and cracking process of non-persistent jointed rocks: An extensive experimental investigation. *Rock Mech. Rock Eng.* **2018**, *51*, 415–428. [CrossRef]
56. Bieniawski, Z.T. Mechanism of brittle fracture of rock, parts 1, II and III. *Int. J. Rock Mech. Min. Geome Abstr.* **1967**, *4*, 395–430.
57. Fakoor, M.; Shahsavar, S. The effect of T-stress on mixed mode I/II fracture of composite materials: Reinforcement isotropic solid model in combination with maximum shear stress theory. *Int. J. Solids Struct.* **2021**, *229*, 111145. [CrossRef]
58. Jiao, Y.; Zuo, Y.; Wen, Z.; Chen, Q.; Zheng, L.; Lin, J.; Chen, B.; Rong, P.; Jin, K.; Du, S. Crack-tip propagation laws and energy evolution of fractured sandstone. *Eng. Fail. Anal.* **2024**, *166*, 108832. [CrossRef]
59. Sagong, M.; Bobet, A. Coalescence of multiple flaws in a rock-model material in uniaxial compression. *Int. J. Rock Mech. Min.* **2002**, *39*, 229–241. [CrossRef]
60. Cui, Y.; Xu, C.; Chen, H.; Cui, Y.; Xue, L.; Qin, S. Startup mechanism of locked segment-dominated rockslides: Insights from a physical model experiment replicating natural infiltration conditions. *Eng. Geol.* **2026**, *364*, 108494. [CrossRef]
61. Hoek, E.; Martin, C.D. Fracture initiation and propagation in intact rock-A review. *J. Rock Mech. Geotech.* **2014**, *6*, 287–300. [CrossRef]

62. Ramsey, J.M.; Chester, F.M. Hybrid fracture and the transition from extension fracture to shear fracture. *Nature* **2004**, *428*, 63–66. [CrossRef] [PubMed]
63. Renani, H.; Cai, M. Forty-Year Review of the Hoek–Brown Failure Criterion for Jointed Rock Masses. *Rock Mech. Rock Eng.* **2022**, *55*, 439–461. [CrossRef]

Disclaimer/Publisher's Note: The statements, opinions and data contained in all publications are solely those of the individual author(s) and contributor(s) and not of MDPI and/or the editor(s). MDPI and/or the editor(s) disclaim responsibility for any injury to people or property resulting from any ideas, methods, instructions or products referred to in the content.